

Enhancing Arsenate Removal Efficiency using Seawater Bittern-Derived MgO Nanoparticles/PVDF-HFP Electrospun Nanofiber Composites

(Meningkatkan Kecekapan Penyingkiran Arsenat menggunakan Nanozarah Air Laut Terbitan-Bittern MgO/Komposit Nanozarah Elektroputaran PVDF-HFP)

ASNAN RINOVIAN^{1,5,*}, MUHAMAD NASIR², MUHAMMAD ALI ZULFIKAR³, SWASMI PURWAJANTI², NUGRAHA^{1,4},
NURRAHMI HANDAYANI^{2,3}, I GUSTI AGUNG SURADHARMIKA⁶ & FITRI DARA²

¹Master Program in Nanotechnology, Institut Teknologi Bandung, 40132, Bandung, Indonesia

²Research Center for Environmental and Clean Technology, National Research and Innovation Agency (BRIN), 40135, Bandung, Indonesia

³Department of Chemistry, Institut Teknologi Bandung, 40132, Bandung, Indonesia

⁴Department of Engineering Physics, Institut Teknologi Bandung, 40132, Bandung, Indonesia

⁵Research Center for Mining Technology, National Research and Innovation Agency (BRIN), 35361, Lampung, Indonesia

⁶Research Center for Advanced Materials, National Research and Innovation Agency (BRIN), 15314, Banten, Indonesia

Received: 30 May 2023/Accepted: 13 July 2023

ABSTRACT

MgO nanoparticles (MgO NPs) incorporated PVDF-HFP nanofibers have been synthesized using the electrospinning method to remove arsenic from polluted water. MgO nanoparticles were synthesized from seawater bitterns and used as magnesium precursors. The synthesized materials were characterized using various techniques, and their adsorption capacities were evaluated against arsenic under different conditions. The results showed that the maximum adsorption for As(V) adsorption was 41.47 mg g⁻¹ for PVDF-HFP/MgO 30% (w/w), which equals 179.69 mg g⁻¹ based on the weight of bare MgO NPs and achieved at pH 11, a contact time of 420 minutes, and an adsorbent weight of 0.0125 g. Incorporating MgO NPs into the nanofiber matrix can enhance its stability, further increase the adsorption capacity. This study demonstrates the potential of using PVDF-HFP/MgO nanofiber composites to treat arsenic-containing wastewater and further provide commercial benefits for seawater bitterns by serving as a precursor for producing functional nanomaterials.

Keywords: Arsenic removal; MgO nanoparticles; nanofiber composites; PVDF-HFP nanofibers; seawater bittern

ABSTRAK

Nanozarah MgO (MgO NPs) yang tergabung PVDF-HFP nanozarah telah disintesis menggunakan kaedah pemintalan elektrik untuk mengeluarkan arsenik daripada air tercemar. Nanozarah MgO telah disintesis daripada bittern air laut dan digunakan sebagai prekursor magnesium. Bahan yang disintesis telah dicirikan menggunakan pelbagai teknik dan kapasiti penjerapannya dinilai terhadap arsenik di bawah keadaan yang berbeza. Hasil menunjukkan bahawa penjerapan maksimum bagi penjerapan As(V) ialah 41.47 mg g⁻¹ untuk PVDF-HFP/MgO 30% (w/w) yang bersamaan dengan 179.69 mg g⁻¹ berdasarkan berat NP MgO kosong dan dicapai pada pH 11, masa sentuhan 420 minit dan berat penjerap 0.0125 g. Mencampurkan NP MgO ke dalam matriks nanozarah boleh meningkatkan kestabilannya, seterusnya meningkatkan kemampuan penjerapan. Kajian ini menunjukkan potensi penggunaan komposit nanozarah PVDF-HFP/MgO untuk merawat air sisa yang mengandungi arsenik dan seterusnya memberikan faedah komersial untuk bittern air laut dengan berfungsi sebagai pendahulu untuk menghasilkan bahan nano berfungsi.

Kata kunci: Bittern air laut; komposit nanozarah; nanopartikel MgO; penyingkiran arsenik; PVDF-HFP nanozarah

INTRODUCTION

The presence of arsenic in natural waters is a worldwide issue and poses a continuous challenge for scientists due to strict ecological tolerance levels and concentration limits. The World Health Organization (WHO) has set a maximum arsenic concentration level of $10 \mu\text{g L}^{-1}$ for drinking water (Ng et al. 2001). Inorganic forms of arsenic, such as arsenite (As(III)) (H_2AsO_3^- and H_2AsO_3^-) and arsenate (As(V)) (H_2AsO_4^- and HAsO_4^{2-}), are the primary contaminants found in drinking water (Pramanik et al. 2014). Both arsenite and arsenate are rapidly and extensively absorbed in the gastrointestinal tract (Kwok et al. 2018). Several methods have been developed to remove arsenic from water, including chemical precipitation (Kumar, Nandi & Pakshirajan 2021), coagulation, and flocculation (Peydayesh et al. 2021), biological processes (Meena, Sonigra & Yadav 2021), ion exchange (Arshid et al. 2019), process oxidation (Zhao et al. 2021), and adsorption (Fiyadh et al. 2019). Compared to other methods developed for removing arsenic from drinking water, adsorption is an attractive alternative due to its easy operation, low cost, and high adsorption capabilities, making it the preferred choice (De Gisi et al. 2016; Shafiq, Alazba & Amin 2018; Siti Zu Nurain et al. 2021).

Nanomaterials have recently gained popularity as adsorbents for heavy metals in water treatment processes. Some examples of such materials include iron oxide (Mohammadian et al. 2021), manganese dioxide (Delavar et al. 2021), titanium dioxide (Liao et al. 2021), zinc oxide (Siti Zu Nurain et al. 2021), and magnesium oxide (MgO) (Gupta et al. 2021). MgO nanoparticles (MgO NPs) are widely used for removing heavy metals like lead, nickel, cadmium, and arsenic and are advantageous due to their natural abundance, non-toxicity, and environmental friendliness (Guo et al. 2022; Saod et al. 2023; Xiong et al. 2015). Due to high concentration of Mg^{2+} , seawater bittern show a great potency as Mg^{2+} precursor in the preparation of MgO NPs. Using seawater bittern as the Mg^{2+} precursor in the precipitation method offers cost-effective and sustainable manufacturing, repurposing a byproduct and minimizing waste generation while conserving resources (Apriani, Hadi & Masduqi 2018; Davies & Knowles 2006; Lim et al. 2022).

Seawater bittern can contain various impurities, such as other metal ions, organic compounds, or particulate matter. These impurities may have both beneficial and detrimental effects on the synthesized nanoparticles. Impurities can act as dopants, modifying

properties, but can also introduce defects in the lattice structure (Araujo, Terrones & Dresselhaus 2012; Yavari et al. 2019).

Although MgO NPs has been found to have a high capacity for adsorbing arsenic, surpassing other metal oxides (Luo & Deng 2019), its effectiveness as an adsorbent is hindered by various challenges during application. When used in water treatment, the nano-sized adsorbents tend to aggregate, leading to reduced adsorption capacity. Furthermore, separating the adsorbent from the water after the complete process presents further issues. To address these challenges, researchers have developed nanomaterial adsorbents incorporated with polymer host media (D. Perez et al. 2017; Shi et al. 2021).

Due to their unique characteristics, such as their porous structure and high mechanical strength, electrospun nanofiber materials have recently been created for water purification (Gupta et al. 2015). Polyvinylidene fluoride (PVDF) has been studied extensively for its advantageous properties, such as high thermal stability, good mechanical strength, and chemical resistance to some organic solvents, acids, and bases. Compared to other fluoropolymers, PVDF can quickly dissolve in most organic solvents (Gopakumar et al. 2017). PVDF can also be combined with other polymers to form copolymers with superior properties. One of the PVDF copolymers that have been widely developed is PVDF-HFP (polyvinylidene fluoride-co-hexafluoropropylene) which has high flexibility and stability, good mechanical strength, and is relatively easy to process (Lin et al. 2022; Puguan, Chung & Kim 2016). It has even been used as a matrix to treat heavy metal waste (Pi et al. 2018). Recent developments in nanofiber materials synthesized by electrospinning have led to the production of unique materials with desirable properties for water purification.

In this study, MgO NPs was prepared from seawater bittern (by product of saltwork production) as a sustainable source of magnesium ions using an environmentally friendly precipitation process and incorporated into polymer matrix PVDF-HFP nanofiber using the electrospinning method. This is the first reported of bittern-derived MgO nanoparticles/PVDF-HFP electrospun nanofiber composites for arsenic sequestration. The incorporation of MgO NPs into the matrix of PVDF-HFP nanofiber is expected to reduce the aggregation and enhance the stability of MgO NPs, which results in the enhanced adsorption capacity toward arsenic and more easily separated from water

when the adsorption process is complete. Moreover, we have conducted metal arsenic adsorption tests, where we studied the effects of several parameters, including solution pH, contact time, adsorbent dose, and arsenic ion concentration, and have shown promising results, indicating that this material has great potential for efficient water purification. Our study aims to contribute to the rational design of functional material for water purification, which is of great importance in addressing the growing concerns about water pollution and scarcity.

MATERIALS AND METHODS

MATERIALS

Polyvinylidene fluoride co-hexafluoro propylene (PVDF-HFP, Arkema Kynar Flex 2801-00), N,N-Dimethylacetamide (DMAc), ethanol, sodium hydroxide (NaOH), and disodium hydrogen arsenate ($\text{Na}_2\text{HAsO}_4 \cdot 7\text{H}_2\text{O}$) were purchased from Merck. Deionized (DI) water was used during this study. Seawater bitterns (SWBs) were collected from saltponds in Madura, Indonesia. All the chemicals were used as received without further purification.

PREPARATION OF ADSORBENT

SYNTHESIS OF MGO NANOPARTICLES

Two mol NaOH was slowly dripped into 1 mol SWBs (containing 58 g L^{-1} of magnesium) at a flow rate of 11 mL min^{-1} and stirred with a magnetic stirrer for 30 min at room temperature. The mixture was then centrifuged at 3000 rpm for 15 min. The presence of impurities in seawater bittern necessitates careful control and removal steps during the synthesis process. Proper purification techniques may be employed to minimize the impurity content and ensure the desired purity of the MgO nanoparticles. The solid phase was washed twice with ethanol and hot water at $80 \text{ }^\circ\text{C}$ to remove impurities and dried at $60 \text{ }^\circ\text{C}$ overnight. The products identified

as $\text{Mg}(\text{OH})_2$ were calcined to produce MgO at $400 \text{ }^\circ\text{C}$ for five hours at a target temperature with a temperature increase of $2 \text{ }^\circ\text{C per min}$.

SYNTHESIS OF PVDF-HFP/MGO NANOFIBER COMPOSITES

PVDF-HFP copolymer 24% (w/v) was dissolved in 10 mL of DMAc and stirred with a magnetic stirrer for 5 h. The synthesized MgO nanoparticles were then added with variations in weight (w/w) against the weight of the PVDF-HFP copolymer into the copolymer solution and stirred for $\pm 12 \text{ h}$. The sample composition is shown in Table 1. The solution was then put into the syringe and spun using an electrospinning device with a flow rate of $16.67 \text{ } \mu\text{L min}^{-1}$, a distance from the nozzle to the collector of 17 cm, and a voltage of 21 kV for a duration of 4 h. The nanofiber was collected on an aluminum foil.

CHARACTERIZATION OF ADSORBENT

The synthesized MgO NPs, PVDF-HFP nanofibers, and PVDF-HFP/MgO nanofiber composites were characterized by using X-Ray Diffraction (XRD) (Bruker D8 Advance, Germany) with $\text{Cu K}\alpha$ as a radiation source ($\lambda: 1.540 \text{ \AA}$) at a diffraction angle of 2θ from 10° - 90° . An attenuated total reflection-Fourier transform infrared (ATR-FTIR) spectrophotometer was used at wavenumber 4000 - 400 cm^{-1} to analyze the functional groups of the adsorbents. The JEOL-JSM IT-300 scanning electron microscope (SEM) was used for the morphological analysis of the adsorbent. Samples were observed at a magnification of 30,000 times. The elemental composition of the nanofibers was characterized using Energy Dispersive X-Ray Spectroscopy (EDS). A Hitachi HT7700 transmission electron microscope (TEM) was used to identify the detailed internal structure of the adsorbent in high resolution. The N_2 adsorption-desorption (BET) surface area analyzer (Nova 3200e Quantachrome) was used to determine the surface area of the adsorbent.

TABLE 1. Composition of PVDF-HFP nanofiber and PVDF-HFP/MgO nanofiber composites

Sample type	PVDF-HFP copolymer (% w/v)	MgO nanoparticles (% w/w)
PVDF-HFP	24	0
PVDF-HFP/MgO 10%	24	10
PVDF-HFP/MgO 20%	24	20
PVDF-HFP/MgO 30%	24	30

BATCH ADSORPTION STUDIES

In this study, the effect of pH, contact time, adsorbent dosage, and initial concentration of arsenic on the adsorption capacity of the adsorbent was studied using the batch method. The study on the effect of pH was carried out by contacting 0.05 g (cut in small pieces) of PVDF-HFP nanofiber and PVDF-HFP/MgO composite nanofiber with 10 mL of As(V) solution with a concentration of 100 mg L⁻¹ with variations in pH of 3, 5, 7, 9 and 11, then stirred for 24 h on a shaker at 150 rpm. After that, the mixture was filtered, the filtrate was collected, and the As(V) ion concentration was measured after adsorption using AAS. The amount of adsorbed As(V) ions at equilibrium (q_e) is calculated using Equation (1):

$$q_e = \frac{C_i - C_e}{m} V \quad (1)$$

where q_e is the adsorption capacity; V is the volume of the solution (L); m is the mass of the adsorbent (g); C_i and C_e are the initial and final concentrations of As(V) (mg L⁻¹), respectively.

To evaluate the effect of contact time, 0.05 g of PVDF-HFP nanofiber and PVDF-HFP/MgO composite nanofiber were contacted with 10 mL of 100 mg L⁻¹ As(V) solution with various contact times of 30, 60, 90, 120, 180, 240, 300, 360, 420, and 480 min at optimum pH. To evaluate the effect of adsorbent mass, contacting 10 mL of 100 mg L⁻¹ As(V) solution was contacted to variations in adsorbent masses of 0.00625, 0.0125, 0.01875, 0.025, and 0.05 g at optimum pH and contact time. Meanwhile, studies on the effect of the initial concentration of As(V) ions were carried out at concentrations of 10, 20, 40, 60, 80, 100, and 150 mg L⁻¹ at optimum pH, contact time, and adsorbent mass.

STABILITY STUDIES

The study was carried out by incorporating a certain amount of adsorbent with the same weight of MgO NPs into distilled water at various pHs 3, 5, 7, 9, and 11. Then it was stirred for 24 h, the adsorbent was separated from the water, and the Mg ion concentration released into the medium was measured using AAS.

RESULTS AND DISCUSSION

CHARACTERIZATION OF MgO NPs AND PVDF-HFP/MgO COMPOSITE NANOFIBER

MgO NPs were synthesized by precipitation method employing seawater bittern as Mg²⁺ precursor. The morphology of MgO NPs was identified using SEM spectroscopy. Figure 1(a) shows that the particle size range of MgO NPs is 33-51 nm, and the agglomeration of the samples was further confirmed from the SEM image. TEM image showed that the shape of single MgO NPs was a flake-like structure (Figure 1(b)). The agglomeration observed in the SEM image may pose challenges in applying these nanoparticles as an adsorbent, as it can reduce their surface area and adsorption capacity.

Nanofibers were synthesized for a duration of 4 h under specific experimental conditions, including a flow rate of 16.67 $\mu\text{L min}^{-1}$, a distance from the nozzle to the collector of 17 cm, and an applied voltage of 21 kV. Further SEM analysis was also used to study the morphology of the nanofibers and their average distribution. The results depicted in Figure 2(a) show that the morphology of pure PVDF-HFP nanofibers forms straight primary fibers, which were ultrafine and continuous, with no beading detected, although not uniform. SEM images of PVDF-HFP/MgO nanofiber

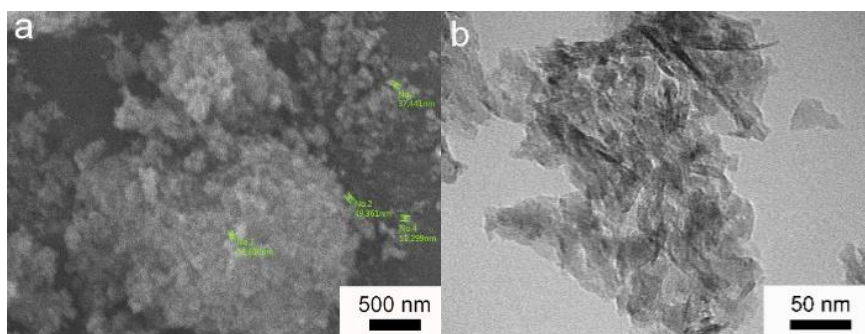


FIGURE 1. Image of (a) SEM MgO NPs at 30,000 times magnification and (b) TEM MgO NPs at 100,000 times magnification

composites with varying concentrations of MgO NPs were also captured, as shown in Figure 2(b)-2(d)). The addition of MgO NPs impacted the size of the nanofibers formed. The figure demonstrates that more beads were formed as more MgO NPs were added, and the MgO NPs were trapped between the nanofiber matrices.

In the electrospinning process for nanofiber characterization, several parameters influence the morphology and diameter distribution of the nanofibers. The applied voltage, typically ranging from a few kilovolts to tens of kilovolts, creates an electric field that promotes the stretching and elongation of the polymer solution. The solution flow rate, controlled by the syringe pump, determines the rate at which the polymer solution is ejected through the needle. The distance between the needle and collector, typically in the range

of a few centimeters to tens of centimeters, affects the stretching and solidification of the ejected polymer solution into nanofibers. These parameters play a crucial role in controlling the diameter, alignment, and overall morphology of the electrospun nanofibers (Ibrahim & Klingner 2020; Veerabhadraiah et al. 2017).

The nanofibers' size distribution and average diameter were determined using ImageJ software. Figure 2 illustrates the size distribution of the resulting fiber diameters. The PVDF-HFP nanofibers had a heterogeneous diameter size ranging from 300 nm to 1 μm , with a predominance of sizes in the range of 500-600 nm (Figure 2(a)). On the other hand, the diameter of the PVDF-HFP/MgO 10% nanofiber composites ranged from 0-700 nm, with a predominance in size of 200-300 nm (Figure 2(b)). The diameter size distribution

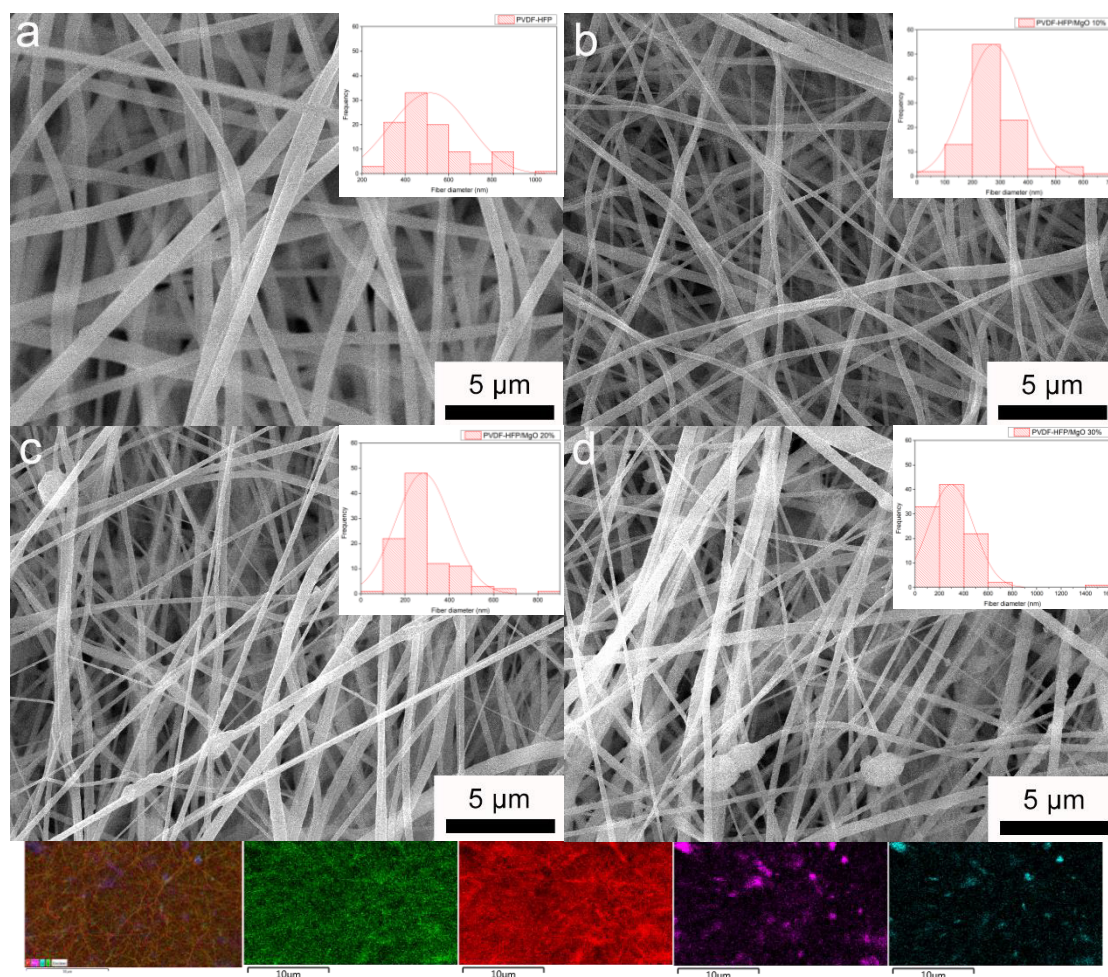


FIGURE 2. SEM images of (a) pure PVDF-HFP nanofiber and PVDF-HFP/MgO composite nanofiber with various MgO NPs concentrations of (b) 10% (w/w), (c) 20% (w/w), (d) 30% (w/w) at 5,000 times magnification, and (e) EDS Mapping of PVDF-HFP/MgO 30% (w/w) nanofiber composites

of PVDF-HFP/MgO 10% nanofiber composites was smaller than that of PVDF-HFP nanofibers. The PVDF-HFP/MgO 20% nanofiber composites had a diameter size distribution in the range of 0-900 nm, with a predominance of sizes in the 200-300 nm (Figure 2(c)). For the PVDF-HFP/MgO 30% nanofiber composites (Figure 2(d)), the diameter size distribution was in the range of 0-1600 nm, with dominance in the size range of 200-400 nm. The data indicate that the size distribution of the nanofibers increased with the addition of MgO NPs. Additionally, Figure S1 shows the calculation results for the average diameter of nanofiber composites in more detail.

Figure S1 presents the relationship between the addition of MgO NPs and the resulting nanofibers' average diameter. It is found that the diameter of PVDF-HFP nanofibers can be further controlled by the addition of MgO NPs. It was observed that after adding 10% (w/w) MgO NPs, the average diameter of PVDF-HFP nanofiber decreased from 515 ± 156 nm to 276 ± 101 nm. This suggests that adding MgO NPs increased the conductivity of the polymer solution (Figure S2), resulting in a smaller fiber diameter due to jet elongation (Yalcinkaya, Yalcinkaya & Jirsak 2015). However, as the amount of MgO NPs increased, the average diameter also increased (282 ± 125 nm for PVDF-HFP/MgO 20% nanofibers and 296 ± 184 nm for PVDF-HFP/MgO 30% nanofibers).

The increase in diameter can be affected by the viscosity of the solution. Adding MgO NPs increased the concentration and viscosity of the solution (Figure S3). This causes more polymer solution to be transferred per jet, making the nanofiber diameter larger (Yalcinkaya, Yalcinkaya & Jirsak 2015). In addition, the viscosity of the polymer solution is also an important factor affecting the morphology of nanofibers. As the polymer solution's viscosity increases, the jet's elongation during the electrospinning process becomes more difficult, leading to the formation of larger fibers. Moreover, the viscosity of the solution is closely related to the concentration of polymer and solvent used in the electrospinning process. Therefore, it is important to carefully control the solution viscosity when synthesizing nanofiber composites to obtain the desired diameter size and morphology.

Using ImageJ software for determining the size distribution and average diameter of nanofibers offers several advantages. Firstly, ImageJ is a widely used and accessible image analysis software with a user-friendly interface, making it accessible to researchers with

varying levels of expertise. It provides a range of image processing and analysis tools that can be customized to specific requirements. Additionally, ImageJ allows for batch processing, enabling efficient analysis of large datasets (Schroeder et al. 2021). However, there are also limitations to consider. ImageJ relies heavily on the quality of the captured images, and poor image quality can introduce errors and uncertainties in size measurements. Segmentation errors may occur, particularly when dealing with complex or overlapping structures. Orientation bias is another potential limitation when analyzing 2D images of anisotropic nanofibers. Calibration accuracy and the potential for user bias in manual adjustments are additional considerations (Huling et al. 2022).

Alternative methods for determining the size distribution and average diameter of nanofibers include scanning electron microscopy (SEM), transmission electron microscopy (TEM), atomic force microscopy (AFM), dynamic light scattering (DLS), X-ray scattering techniques (SAXS/WAXS), and nanoparticle tracking analysis (NTA). SEM and TEM provide high-resolution imaging for direct measurements (Tibolla, Pelissari & Menegalli 2014), while AFM allows for topographic analysis (Wang et al. 2019). DLS measures hydrodynamic size in solution (Mao et al. 2017), X-ray scattering techniques offer structural information (Su et al. 2014), and NTA tracks individual nanoparticles (Amaro-Gahete et al. 2019). Selection depends on nanofiber characteristics and available equipment. Using multiple methods and validating results enhances accuracy and understanding of nanofiber size.

The EDS data provided in Figure S4 complements the SEM image by offering information on the composition of elements in the nanofiber. The EDS spectrum of PVDF-HFP/MgO 10% (Figure S4(d)) and PVDF-HFP/MgO 30% (Figure S4(f)) nanofiber composites displayed the presence of Mg and O elements, which indicated the successful synthesis of composite nanofiber materials. Conversely, pure PVDF-HFP nanofibers contained only C and F elements, as seen in Figure S4(b). Moreover, EDS feature mapping was conducted to confirm the distribution of MgO NPs in the fiber. The results of the EDS mapping of pure PVDF-HFP nanofibers are shown in Figure S5, which shows that the elements C and F are uniformly distributed throughout the scanned area. Figure S6 demonstrates that the constituent elements of MgO NPs, i.e., Mg (purple color) and O (light blue color), are uniformly distributed in the PVDF-HFP/MgO 10% (w/w) composite nanofiber

sample. This characterization indicates that the MgO NPs were well-dispersed in the PVDF-HFP matrix during the electrospinning process, leading to the successful formation of nanofiber composites.

Figure 2(e) shows the presence of Mg (purple color) and O (light blue color), the constituent elements of MgO NPs, in the PVDF-HFP/MgO 30% composite nanofiber. However, it is observed that some elements are agglomerated and trapped between the resulting fibers. The EDS analysis and feature mapping provide crucial information that helps confirm nanofibers' composition and distribution.

Figure 3 shows the X-ray diffraction pattern of the synthesized MgO nanoparticles, the pure PVDF-HFP nanofiber, and the nanofiber composites. The XRD pattern of MgO nanoparticles (Figure 3(a)) shows several peaks at different diffraction angles, indicating the formation of the nanoparticles. The peaks at 36.86° , 42.78° , 62.15° , 74.42° , and 78.41° (ICDD/PDF No. 01-071-1176) correspond to the crystal planes [111], [200], [220], [311], and [222], respectively (Anam et al. 2018). The XRD pattern of pure PVDF-HFP nanofiber (Figure 3(b)) shows several peaks at different diffraction angles, including 18.30° , 20.53° , and 39.26° (ICDD/PDF No. 00-061-1406), indicating the crystal planes [100], [020], and [021], respectively. This suggests that PVDF-HFP is a semicrystalline polymer (Manuel Stephan & Nahm 2006). The XRD pattern of the nanofiber composites (Figure 3(c)-3(e)) confirms the successful synthesis of the PVDF-HFP/MgO nanofiber composites. The diffraction angles of 42.80° and 62.27° , which

correspond to the MgO nanoparticles, are observed in the XRD pattern of the 30% PVDF-HFP/MgO composite nanofiber sample (Figure 3(e)).

The synthesis products were analyzed by examining the absorption bands of functional groups in the IR spectrum. The IR spectra of the synthesized MgO nanoparticles, PVDF-HFP nanofiber, and PVDF-HFP/MgO composite nanofiber (Figure 4) exhibited absorption peaks at specific wave numbers. A wave number of 1400 cm^{-1} indicated a C-F stretching vibration, while 1177 cm^{-1} correlated to $-\text{CF}_2-$ stretching vibration, and 1073 cm^{-1} indicated the presence of C-C stretching vibrations. Additionally, the absorption peak at 877 cm^{-1} suggested the presence of an amorphous phase of the PVDF-HFP polymer, while the absorption peaks at 840 cm^{-1} and 600 cm^{-1} indicated the β phase and crystalline phase of the PVDF-HFP polymer, respectively (Vo et al. 2019). The presence of Mg-O stretching vibrations was shown by an absorption peak at 667 cm^{-1} (Anam et al. 2018), with a higher percentage of MgO resulting in a higher absorption peak.

The specific surface area of the material was analyzed using the N_2 adsorption-desorption method. MgO NPs were found to have a specific surface area of $76.22\text{ m}^2\text{ g}^{-1}$. However, after being composited into the nanofiber system, the specific surface area of the BET material decreased, which was attributed to the dominance of the nanofiber as the matrix. Specifically, the specific surface area of the BET nanofiber PVDF-HFP was used as a control, which was found to be $5.173\text{ m}^2\text{ g}^{-1}$. As the amount of MgO NPs in the nanofiber increased, the

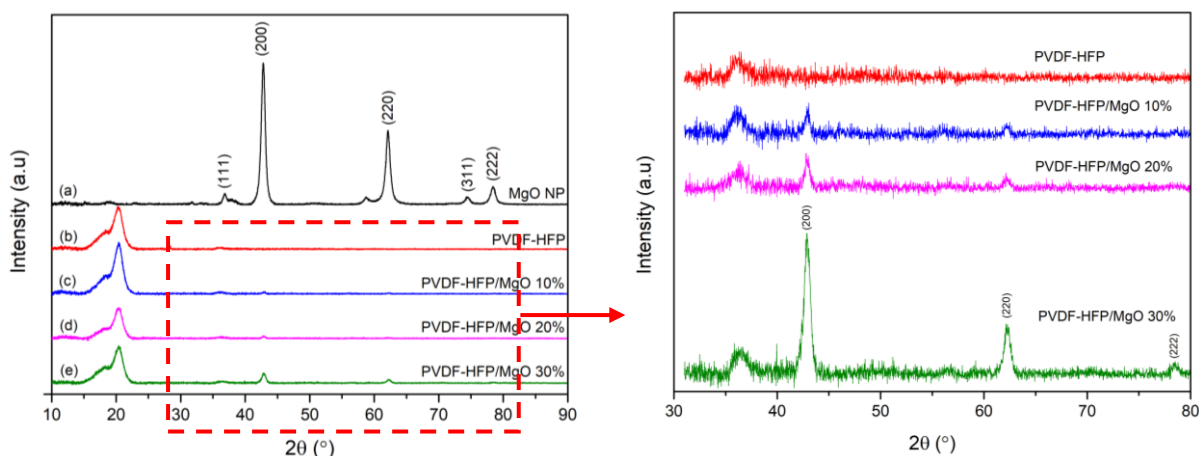


FIGURE 3. XRD Diffractogram of (a) MgO nanoparticles, (b) pure PVDF-HFP nanofiber, and PVDF-HFP/MgO composite nanofiber (c) 10% (w/w), (d) 20% (w/w), (e) 30% (w/w)

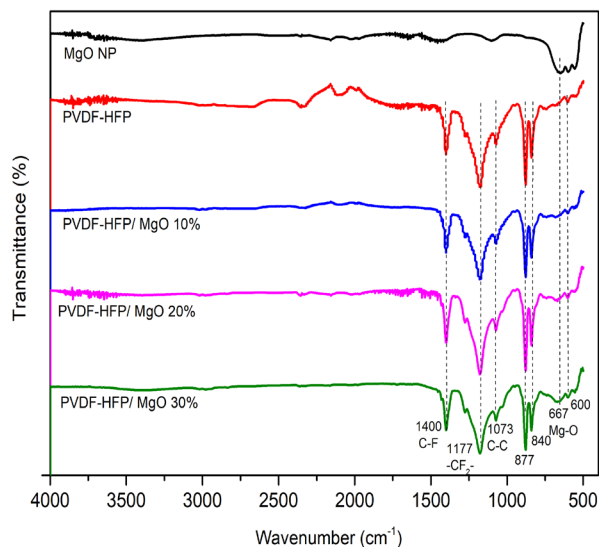


FIGURE 4. IR spectra of MgO nanoparticles, PVDF-HFP nanofibers, and PVDF-HFP/MgO nanofiber composites

BET surface area also increased accordingly. For instance, the specific surface area of the composite increased to $7.301 \text{ m}^2 \text{ g}^{-1}$, $8.147 \text{ m}^2 \text{ g}^{-1}$, and $11.17 \text{ m}^2 \text{ g}^{-1}$ for the 10%, 20%, and 30% composite, respectively. These findings support the theoretical notion that the amount of metal oxide in the nanofiber increases its specific surface area to the optimum loading (Che Othman et al. 2016).

PRELIMINARY STUDY

Before further examining other adsorption parameters, a preliminary study was carried out to determine the adsorption ability of the adsorbent and to select the type of adsorbent to be used in determining the optimum adsorption conditions. The preliminary study was carried out at pH 7 for 24 h; the mass of the adsorbent was 0.05 g, and the initial concentration of As(V) was 100 mg L^{-1} . The value of the equilibrium adsorption capacity (q_e) of each adsorbent is shown in Figure S7. The determination of the q_e value above was calculated based on the total weight of the adsorbent and the weight of MgO NPs as the active agent in the adsorption process. This is because MgO NPs play an important role as an adsorbent for As(V). So that it can also be compared with the same weight of MgO NPs, how is the adsorption ability of MgO NPs when it is in the form of powder and when it is composited into the PVDF-HFP nanofiber matrix.

Based on the equilibrium adsorption capacity (q_e), the 30% PVDF-HFP/MgO composite nanofiber had the

most significant q_e value of 17.85 mg g^{-1} if the weight based on the total weight of the adsorbent (Figure S7(a)). As more MgO NPs are added to the nanofiber, the adsorption capacity increases; this could be due to the increasing BET surface area. However, when the q_e was calculated based on the weight of MgO NPs alone in the composite (Figure S7(b)), 10% PVDF-HFP/MgO composite nanofiber gave the best results with a q_e value of 119.88 mg g^{-1} . Figure S7(b) also shows that as compared to bare MgO NPs, with the same amount of MgO NPs, the PVDF-HFP/MgO nanofiber composites have a higher q_e value than bare MgO NPs. Indicating that incorporating MgO NPs into nanofiber can avoid agglomeration of MgO NPs, making it more effective in adsorbing As(V). Based on these results, samples with 10% and 30% (w/w) MgO NPs percentages were selected for further adsorption studies.

Agglomeration of MgO nanoparticles significantly affects their adsorption capacity by influencing the surface area and accessibility of active sites. When nanoparticles agglomerate, the available surface area for adsorption decreases as the agglomerates form larger structures with reduced specific surface area. Additionally, agglomeration restricts the accessibility of active sites, as they become buried within the agglomerates, hindering the contact between the adsorbate molecules and the active sites (Zhang et al. 2019). To mitigate agglomeration and enhance

dispersion of MgO nanoparticles in nanofiber polymer composites for improved adsorption performance, additional strategies can be employed. One approach is to incorporate the nanoparticles during the electrospinning process, where the nanoparticles are dispersed within the polymer solution prior to fiber formation (Zhang & Yu 2014). This ensures uniform distribution of nanoparticles throughout the nanofiber matrix, minimizing the likelihood of agglomeration. Surface modification of the nanoparticles with polymer coatings can also be utilized in the composite fabrication process, providing enhanced dispersibility and preventing agglomeration. These strategies help to maintain a high surface area and accessibility of active sites within the nanofibers, maximizing their adsorption capacity (Sinha Ray 2021; Zhang et al. 2019).

As(V) ADSORPTION STUDIES

During this step, a known mass of the nanofiber is mixed with the adsorbate solution in a container. The mixture is allowed to equilibrate for a specific period, typically through gentle stirring or shaking, enabling adsorption to take place between the nanofibers and the target adsorbate. The batch test method serves as a straightforward and commonly used approach for the initial evaluation of the adsorption capacities of nanofiber adsorbents. It allows for easy control of experimental parameters and provides valuable data for further optimization and comparison of different nanofiber materials or experimental conditions (Ramlah et al. 2018; Singh et al. 2011; Unuabonah, Omorogie & Oladoja 2018).

EFFECT OF pH

Understanding the impact of pH on the adsorption process is crucial in determining the interaction between the adsorbent and the adsorbate. This study investigated the effect of pH over 24 h, using an adsorbent mass of 0.05 grams and an initial As(V) concentration of 100 mg L⁻¹. Figure 5(a) presents the results of this investigation, demonstrating the effect of pH variations on the equilibrium adsorption capacity.

Figure 5(a) displays the study's findings, indicating that both PVDF-HFP nanofiber and PVDF-HFP/MgO composite nanofiber can adsorb As(V) in a range of pH levels from acidic to alkaline. From this result, it can be inferred that PVDF-HFP nanofiber has a negligible effect on the As(V) adsorption. On the other hand, the

10% and 30% PVDF-HFP/MgO composite nanofiber samples showed optimal pH at pH 11 with q_e values of 11.69 mg g⁻¹ and 20.71 mg g⁻¹, respectively. Therefore, the MgO NPs play a crucial role in the adsorption of As(V) providing the active adsorption sites. The solution's pH variation can impact the observed phenomena by altering the arsenic species, with H₂AsO₄⁻ dominating at pH 6-11, as shown in Figure S8.

Changes in the surface charge of the adsorbent as pH changes can also provide further insight into the observed phenomena. The point zero charge (PZC) value can be used to determine when the surface charge of the adsorbent is zero at a particular pH, known as pH_{PZC}. The pH_{PZC} can also be used to hypothesize the ionization of functional groups and their interactions with metal species in the solution. When the pH of the solution is above pH_{PZC}, the surface of the adsorbent is negatively charged and can interact with positive metal species. Conversely, when the pH is below pH_{PZC}, the surface of the adsorbent is positively charged and can interact with negative metal species (Fiol & Villaescusa 2009; Laili et al. 2010).

According to current literature, there are two general mechanisms for the adsorption of arsenate on a mineral surface: surface complexation and inner-sphere complexation. Surface complexation is the adsorption of arsenate on the surface of MgO starting with the formation of surface complexes. The surface of MgO carries a net positive charge at lower pH values, creating electrostatic attractions with the negatively charged arsenate species. Inner-sphere complexation is arsenate ions that can form inner-sphere complexes with surface Mg(II) sites by replacing hydroxyl groups on the MgO surface. This process involves the coordination of the arsenate oxygens with Mg(II) ions on the surface (Cheng et al. 2009; Cheng et al. 2016).

Figure S9 shows the pH_{PZC} measurements of pure PVDF-HFP nanofiber, MgO nanoparticles, and PVDF-HFP/MgO composite nanofiber, which are 5.8, 12.4, and 12.2, respectively. The pH_{PZC} value impacts the optimal pH of pure PVDF-HFP nanofiber and PVDF-HFP/MgO composite nanofiber, which is 5 and 11, respectively. In the case of pure PVDF-HFP nanofiber, the highest adsorption capacity was achieved at pH 5, which then decreased as pH increased. This is due to the fact that the surface of the adsorbent is positively charged at pH below 5 (<pH_{PZC}) and can interact with negatively charged arsenate species, while at pH above 5 (>pH_{PZC}), the surface of the adsorbent becomes negatively charged.

Similar observations were made for the MgO nanoparticle samples and PVDF-HFP/MgO nanofiber composites. At pH below 12 ($<pH_{pzc}$), the adsorbent surface is positively charged, allowing for interaction with negative arsenate species ($H_2AsO_4^-$ dominating at pH 2-6, and $HAsO_4^{2-}$ dominating at pH 6-11), and adsorption capacity improves with increasing pH as it interacts with the more negative arsenate species.

Higher adsorption capacity at high can also be explained from leaching behaviour of Mg^{2+} at different pH, therefore the leaching of Mg^{2+} was evaluated at different pH. The results showed that with an equivalent amount of MgO, the PVDF-HFP/MgO composite nanofiber leached fewer Mg ions than bare MgO nanoparticles (Figure S10). For instance, at pH 5 and 9, the leached Mg^{2+} were 5.98% and 5.04% on PVDF-HFP/MgO composite nanofiber. In the bare MgO nanoparticles, Mg^{2+} leached more, namely 7.84% and 6.49%.

The adsorption capacity of the PVDF-HFP/MgO composite nanofiber with bare MgO nanoparticles was further measured. As a result, with the same amount of MgO NPs, the PVDF-HFP/MgO nanofiber composites had a higher adsorption capacity than bare MgO nanoparticles. Both had optimum adsorption capacities at pH 11, respectively, 89.76 $mg\ g^{-1}$ and 81.17 $mg\ g^{-1}$ for the PVDF-HFP/MgO and MgO NPs nanofiber composites (Figure S11). This result shows a relationship between adsorption capacity and the amount of Mg^{2+} leach, which govern the stability of PVDF-HFP/MgO. In conclusion, incorporating MgO into the PVDF-HFP copolymer matrix can increase its stability and thus enhance the adsorption capacity.

The leaching of Mg^{2+} from bare MgO nanoparticles and PVDF-HFP/MgO composite nanofibers is a significant factor affecting their stability and long-term performance as adsorbents in water treatment applications. Mg^{2+} leaching can alter the surface chemistry and reactivity of bare MgO nanoparticles, while the presence of a polymer matrix in the composites can delay the release of Mg^{2+} ions (Zhu et al. 2020). However, prolonged exposure to water may still result in gradual leaching. The implications include potential changes in water quality and a reduction in adsorption capacity over time, emphasizing the need for careful consideration of Mg^{2+} leaching in optimizing the adsorbents' performance (He, Li & Ren 2022).

EFFECT OF CONTACT TIME

The objective of studying the variations in contact time is to assess the efficiency and effectiveness of adsorption

by analyzing the equilibrium of the adsorption process at a specific time. The study was carried out with an adsorbent mass of 0.05 gram, an initial concentration of As(V) 100 ppm, and at an optimum pH. According to Figure 5(b), the adsorption capacity of the adsorbent is relatively high within the first 30 min of the adsorption process. This is because many active sites on the adsorbent can still interact with the arsenic ions during this initial period. However, the adsorption capacity gradually decreases over time until it reaches saturation. At this point, the adsorption process reaches equilibrium, characterized by a constant adsorption capacity. For the PVDF-HFP nanofibers, PVDF-HFP/MgO 10% nanofiber composites, and PPVDF-HFP/MgO 30%, the equilibrium is reached at 360, 420, and 360 minutes, respectively.

EFFECT OF ADSORBENT MASS

The purpose of examining the effect of adsorbent mass is to determine the adsorption capacity of the adsorbent for a specific initial concentration of adsorbate. The study was carried out with an initial concentration of As(V) 100 ppm, at an optimum pH and contact time. Figure 5(c) illustrates the impact of increasing the adsorbent mass on the adsorption of As(V) ions. It can be observed that an increase in adsorbent mass results in a larger surface area and more adsorption sites, leading to an increase in the amount of As(V) adsorbed. However, there comes a point where increasing the mass amount of the adsorbent no longer provides a significant increase in adsorption capacity. This point is referred to as the saturation point of the adsorbent, where all adsorption sites on the adsorbent mass are completely filled with the adsorbed substance. Therefore, the optimum adsorbent mass in a certain amount of volume usually reaches the saturation point of the adsorbent (Dong et al. 2018; Nandiyanto, Ragadhita & Yunas 2020). The optimal adsorbent mass for 10 mL of adsorbate volume was 0.025 g for pure PVDF-HFP nanofiber and 0.0125 g for PVDF-HFP/MgO composite nanofiber.

EFFECT OF INITIAL ADSORBATE CONCENTRATION

The study of variations in the initial concentration of the adsorbate aims to determine the efficiency and effectiveness of the adsorption process by observing the equilibrium state at specific concentrations. The study was carried out at an optimum pH, contact time, and adsorbent mass. When the initial concentration is low, the active sites on the adsorbent surface can easily adsorb many metal ions, resulting in a sharp increase in

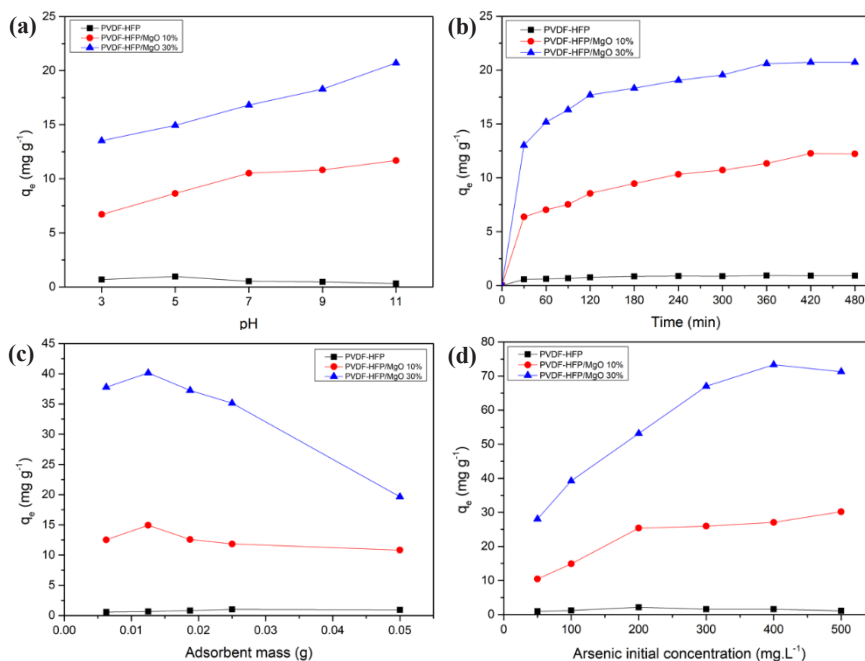


FIGURE 5. Effect of (a) adsorbate pH, (b) contact time, (c) adsorbent mass, and (d) initial concentration of adsorbate on the adsorption capacity of pure PVDF-HFP nanofiber and PVDF-HFP/MgO composite nanofiber

efficiency up to a certain concentration. However, as the initial concentration is further increased, there comes the point where the active sites on the adsorbent surface become saturated, and the available pores are unable to adsorb more metal ions. This can be seen in the test results in Figure 5(d).

ADSORPTION KINETICS

The adsorption kinetic study was performed to evaluate the dynamic binding process of PVDF-HFP/MgO composite nanofiber. This study used two adsorption kinetic models, including pseudo-first and pseudo-second-order kinetic models, to examine the adsorption kinetic model that better fits the adsorption of As(V) ions onto the composite nanofiber. The linear equation of the pseudo-first-order model is expressed as follows:

$$\ln(q_e - q_t) = \ln q_e - k_1 t \quad (2)$$

where k_1 (min^{-1}) is the pseudo-first-order kinetic rate constant, q_t and q_e (mg g^{-1}) are the binding amounts and the equilibrium adsorption capacity of PVDF-HFP/MgO composite nanofiber for As(V) at contact time t (min), respectively.

The linear equation of the pseudo-second-order kinetic model is described as follows:

$$\frac{t}{q_t} = \frac{1}{(k_2 q_e^2)} + \frac{t}{q_e} \quad (3)$$

where k_2 ($\text{g mg}^{-1} \text{min}^{-1}$) represents the pseudo-second-order kinetic rate constant. Figure S12 shows the pseudo-first and pseudo-second-order fitting for pure PVDF-HFP nanofibers, PVDF-HFP/MgO 10%, and PVDF-HFP/MgO 30% nanofiber composites.

The summary of the As(V) adsorption kinetic parameter data is shown in Table S1. According to the table, the value of the equilibrium adsorption capacity of each adsorbent calculated by the pseudo-second-order model is closer to the experimental equilibrium adsorption than the pseudo-first-order model. Therefore, based on the results, the adsorption kinetics of As(V) onto the three types of adsorbents are more in line with pseudo-second-order kinetics with correlation coefficients of 0.995, 0.993, and 0.999 for PVDF-HFP, PVDF-HFP/MgO 10%, and PVDF-HFP/MgO 30%, respectively. Pseudo second order adsorption refers to a type of adsorption kinetics in which the rate of

adsorption of a solute onto a solid surface is proportional to the square of the remaining solute concentration. This means that the rate of adsorption is dependent on the concentration of the solute and the availability of the adsorption sites on the surface of the solid material (Jabar et al. 2020; Noor Halini et al. 2023).

ADSORPTION ISOTHERM

This study used the adsorption isotherm to describe the relationship between the adsorbed masses under specific conditions. To determine the adsorption isotherm, the concentration of the solution before and after adsorption was calculated to measure the amount of adsorbate adsorbed on the adsorbent. Several models can be used to evaluate adsorption equilibrium experimental data. The Langmuir and Freundlich isotherm models were used in this study. Figure 6 shows the fitting of the Langmuir and Freundlich isotherm models based on the results of this study.

Based on the results, the Langmuir isotherm model fits better than the Freundlich isotherm model for

describing the adsorption behavior of As(V) using pure PVDF-HFP nanofiber, 10% PVDF-HFP/MgO composite nanofiber, and 30% PVDF-HFP/MgO composite nanofiber. This is evidenced by the higher correlation coefficients obtained from the Langmuir isotherm model, as seen in Figure 6. The Langmuir model assumes homogeneous adsorption in a monolayer. The number of active sites on the adsorbent surface has the same adsorption energy level, and the adsorbed molecules or ions are adsorbed onto the active sites. The Langmuir and Freundlich adsorption isotherm parameters are presented in Table S2. Adding MgO NPs to the nanofiber increases the adsorption capacity, which is attributed to the increase in the BET surface area.

The adsorption capacities of various adsorbents for As(V) from previous studies are summarized in Table S3. Compared to the maximum adsorption capacity of some previous adsorbents, PVDF-HFP/MgO composite nanofiber can be considered an efficient adsorbent for arsenic removal.

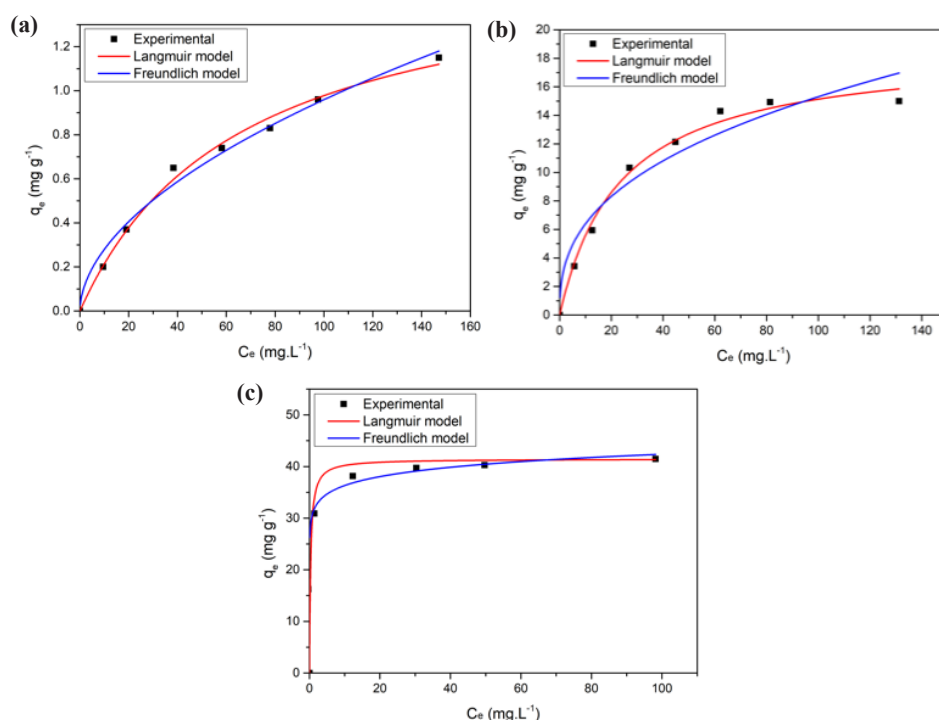


FIGURE 6. Langmuir, Freundlich isotherm model and experimental results of As(V) adsorption on (a) pure PVDF-HFP nanofiber adsorbent, (b) PVDF-HFP/MgO 10% composite nanofiber, and (c) PVDF-HFP/MgO 30% composite nanofiber

CONCLUSIONS

This study successfully synthesized MgO nanoparticles and PVDF-HFP/MgO nanofiber composites, as confirmed through various FTIR, SEM, TEM, EDS, and XRD analyses. The MgO NPs were observed to have an average particle size ranging from 33-51 nm with an average crystallite size of 9.77 nm. The nanoflakes were observed in the form of MgO, and the amount of MgO NPs added will influence the size and diameter of nanofibers. The study identified the optimal conditions for As(V) adsorption using PVDF-HFP/MgO nanofiber composites, and the adsorption process followed the pseudo-second-order and Langmuir isotherm models. Further, it is found that incorporating MgO NPs into the PVDF-HFP copolymer matrix not only can increase its stability but also increase adsorption capacity. Adding MgO NPs to the nanofiber matrix increased the adsorption capacity with a maximum value of 41.47 mg g⁻¹ for 30% PVDF-HFP/MgO composite nanofiber and comparable with other reported works. Overall, these findings can contribute to developing efficient and cost-effective adsorbents for removing arsenic from contaminated water sources, which can significantly impact public health and environmental sustainability.

ACKNOWLEDGEMENTS

The author is very grateful to the National Research and Innovation Agency (BRIN) for this research study's financial, facilities, and technical support. The Department of Chemistry, Institut Teknologi Bandung, for its Atomic Absorption Spectrophotometry (AAS) facilities, and the Research Center for Nanoscience and Nanotechnology (PPNN) ITB for its Transmission Electron Microscope (TEM) facilities.

REFERENCES

- Amaro-Gahete, J., Benítez, A., Otero, R., Esquivel, D., Jiménez-Sanchidrián, C., Morales, J., Caballero, Á. & Romero-Salguero, F.J. 2019. A comparative study of particle size distribution of graphene nanosheets synthesized by an ultrasound-assisted method. *Nanomaterials* 9(2): 152. <https://doi.org/10.3390/nano9020152>
- Anam Ansari, Abad Ali, Mohd Asif & Shamsuzzaman. 2018. Microwave-assisted MgO NP catalyzed one-pot multicomponent synthesis of polysubstituted steroidal pyridines. *New Journal of Chemistry* 42(1): 184-197. <https://doi.org/10.1039/c7nj03742b>
- Apriani, Mirna, Wahyono Hadi & Ali Masduqi. 2018. Physicochemical properties of sea water and bittern in Indonesia: Quality improvement and potential resources utilization for marine environmental sustainability. *Journal of Ecological Engineering* 19(3): 1-10. <https://doi.org/10.12911/22998993/86150>
- Araujo, P.T., Terrones, M. & Dresselhaus, M.S. 2012. Defects and impurities in graphene-like materials. *Materials Today* 15(3): 98-109.
- Arshid Bashir, Lateef Ahmad Malik, Sozia Ahad, Taniya Manzoor, Mudasir Ahmad Bhat, G.N. Dar & Altaf Hussain Pandith. 2019. Removal of heavy metal ions from aqueous system by ion-exchange and biosorption methods. *Environmental Chemistry Letters* Springer. <https://doi.org/10.1007/s10311-018-00828-y>
- Babae, Y., Mulligan, C.N. & Rahaman, M.S. 2018. Removal of arsenic (III) and arsenic (V) from aqueous solutions through adsorption by Fe/Cu nanoparticles. *Journal of Chemical Technology and Biotechnology* 93(1): 63-71. <https://doi.org/10.1002/jctb.5320>
- Che Othman, F.E., Yusof, N., Jaafar, J., Ismail, A.F., Hasbullah, H., Abdullah, N. & Ismail, M.S. 2016. Preparation and characterization of polyacrylonitrile/manganese dioxides-based carbon nanofibers via electrospinning process. In *IOP Conference Series: Earth and Environmental Science*. 36: 012006. <https://doi.org/10.1088/1755-1315/36/1/012006>
- Cheng, H., Hu, Y., Luo, J., Xu, B. & Zhao, J. 2009. Geochemical processes controlling fate and transport of arsenic in acid mine drainage (AMD) and natural systems. *Journal of Hazardous Materials* 165(1-3): 13-26. <https://doi.org/10.1016/j.jhazmat.2008.10.070>
- Cheng, W., Zhang, W., Hu, L., Ding, W., Wu, F. & Li, J. 2016. Etching synthesis of iron oxide nanoparticles for adsorption of arsenic from water. *RSC Advances* 6(19): 15900-15910. <https://doi.org/10.1039/c5ra26143k>
- Cruz, G.J.F., Mondal, D., Rimaycuna, J., Soukup, K., Gómez, M.M., Solis, J.L. & Lang, J. 2020. Agrowaste derived biochars impregnated with ZnO for removal of arsenic and lead in water. *Journal of Environmental Chemical Engineering* 8(3). <https://doi.org/10.1016/j.jece.2020.103800>
- D. Perez, J.V., Nades, E.T., Nguyen, H.N., P. Dalida, M.L. & Rodrigues, D.F. 2017. Response surface methodology as a powerful tool to optimize the synthesis of polymer-based graphene oxide nanocomposites for simultaneous removal of cationic and anionic heavy metal contaminants. *RSC Advances* 7(30): 18480-18490. <https://doi.org/10.1039/c7ra00750g>
- Davies, P.A. & Knowles, P.R. 2006. Seawater bitters as a source of liquid desiccant for use in solar-cooled greenhouses. *Desalination* 196(1-3): 266-279. <https://doi.org/10.1016/j.desal.2006.03.010>

- De Gisi, S., Lofrano, G., Grassi, M. & Notarnicola, M. 2016. Characteristics and adsorption capacities of low-cost sorbents for wastewater treatment: A review. *Sustainable Materials and Technologies* 9: 10-40. <https://doi.org/10.1016/j.susmat.2016.06.002>
- Delavar, M., Bakeri, Gh., Hosseini, M. & Nabian, N. 2021. Synthesis and application of titania nanotubes and hydrous manganese oxide in heavy metal removal from aqueous solution: Characterization, comparative study, and adsorption kinetics. *Theoretical Foundations of Chemical Engineering* 55(1): 180-197. <https://doi.org/10.1134/S004057952101005X>
- Dong, J., Xu, F., Dong, Z., Zhao, Y., Yan, Y., Jin, H. & Li, Y. 2018. Fabrication of two dual-functionalized covalent organic polymers through heterostructural mixed linkers and their use as cationic dye adsorbents. *RSC Advances* 8(34): 19075-19084. <https://doi.org/10.1039/c8ra01968a>
- Fiol, N. & Villaescusa, I. 2009. Determination of sorbent point zero charge: Usefulness in sorption studies. *Environmental Chemistry Letters* 7(1): 79-84. <https://doi.org/10.1007/s10311-008-0139-0>
- Fiyadh, S.S., AlSaadi, M.A., Jaafar, W.Z., AlOmar, M.K., Fayaed, S.S., Mohd, N.S., Lai, S.H. & El-Shafie, A. 2019. Review on heavy metal adsorption processes by carbon nanotubes. *Journal of Cleaner Production* 230: 783-793. <https://doi.org/10.1016/j.jclepro.2019.05.154>
- Gopakumar, D.A., Pasquini, D., Henrique, M.A., De Moraes, L.C., Grohens, Y. & Thomas, S. 2017. Meldrum's acid modified cellulose nanofiber-based polyvinylidene fluoride microfiltration membrane for dye water treatment and nanoparticle removal. *ACS Sustainable Chemistry and Engineering* 5(2): 2026-2033. <https://doi.org/10.1021/acssuschemeng.6b02952>
- Guo, J., Yan, C., Luo, Z., Fang, H., Hu, S. & Cao, Y. 2019. Synthesis of a novel ternary HA/Fe-Mn oxides-loaded biochar composite and its application in cadmium(II) and arsenic(V) adsorption. *Journal of Environmental Sciences (China)* 85: 168-176. <https://doi.org/10.1016/j.jes.2019.06.004>
- Guo, Q., Li, Y., Wei, X.Y., Zheng, L.W., Li, Z.Q., Zhang, K.G. & Yuan, C.G. 2021. Electrospun metal-organic frameworks hybrid nanofiber membrane for efficient removal of As(III) and As(V) from water. *Ecotoxicology and Environmental Safety* 228: 112990. <https://doi.org/10.1016/j.ecoenv.2021.112990>
- Guo, L., Lei, R., Zhang, T.C., Du, D. & Zhan, W. 2022. Insight into the role and mechanism of polysaccharide in polymorphous magnesium oxide nanoparticle synthesis for arsenate removal. *Chemosphere* 296: 133878. <https://doi.org/10.1016/j.chemosphere.2022.133878>
- Gupta, K., Joshi, P., Gusain, R. & Khatri, O.P. 2021. Recent advances in adsorptive removal of heavy metal and metalloid ions by metal oxide-based nanomaterials. *Coordination Chemistry Reviews* 445: 214100. <https://doi.org/10.1016/j.ccr.2021.214100>
- Gupta, R., Kumar, R., Sharma, A. & Verma, N. 2015. Novel Carbon nanofiber composites for the counter electrodes of dye-sensitized solar cells. *International Journal of Energy Research* 39(5): 668-680. <https://doi.org/10.1002/er.3279>
- He, Q., Li, X. & Ren, Y. 2022. Analysis of the simultaneous adsorption mechanism of ammonium and phosphate on magnesium-modified biochar and the slow release effect of fertiliser. *Biochar* 4: 25. <https://doi.org/10.1007/s42773-022-00150-5>
- Huling, J., Götz, A., Grabow, N. & Illner, S. 2022. GIFT: An ImageJ macro for automated fiber diameter quantification. *PLoS ONE* 17(10): e0275528. <https://doi.org/10.1371/journal.pone.0275528>
- Ibrahim, H.M. & Klingner, A. 2020. A review on electrospun polymeric nanofibers: Production parameters and potential applications. *Polymer Testing* 90: 106647. <https://doi.org/10.1016/j.polymertesting.2020.106647>
- Jabar, J.M., Odusote, Y.A., Alabi, K.A. & Ahmed, I.B. 2020. Kinetics and mechanisms of congo-red dye removal from aqueous solution using activated *Moringa oleifera* seed coat as adsorbent. *Applied Water Science* 10: 136. <https://doi.org/10.1007/s13201-020-01221-3>
- Kumar, M., Nandi, M. & Pakshirajan, K. 2021. Recent advances in heavy metal recovery from wastewater by biogenic sulfide precipitation. *Journal of Environmental Management* 278 (Part 2): 111555. <https://doi.org/10.1016/j.jenvman.2020.111555>
- Kwok, K.C.M., Koong, L.F., Al Ansari, T. & McKay, G. 2018. Adsorption/desorption of arsenite and arsenate on chitosan and nanochitosan. *Environmental Science and Pollution Research* 25(15): 14734-14742. <https://doi.org/10.1007/s11356-018-1501-9>
- Kwok, K.C.M., Koong, L.F., Al Ansari, T. & McKay, G. 2018. Adsorption/desorption of arsenite and arsenate on chitosan and nanochitosan. *Environmental Science and Pollution Research* 25(15): 14734-14742. <https://doi.org/10.1007/s11356-018-1501-9>
- Laili, Zalina, Muhamad Samudi Yasir, Muhamat Omar, Mohd Zaidi Ibrahim, and Esther Philip. 2010. Influence of humic acids on radium adsorption by coir pith in aqueous solution. *Sains Malaysiana* 39(1): 99-106.
- Liao, J., Zhang, Y., He, X., Zhang, L. & He, Z. 2021. The synthesis of a novel titanium oxide aerogel with highly enhanced removal of uranium and evaluation of the adsorption mechanism. *Dalton Transactions* 50(10): 3616-3628. <https://doi.org/10.1039/d0dt04320f>
- Lim, J., Kim, D.J., Cho, H. & Kim, J. 2022. Design of novel seawater bittern recovery process for CO₂ and SO_x utilization. *Desalination* 540. <https://doi.org/10.1016/j.desal.2022.115995>
- Lin, S., Tang, J., Zhang, W., Zhang, K., Chen, Y., Gao, R., Yin, H., Yu, X. & Qin, L.C. 2022. Facile preparation of flexible binder-free graphene electrodes for high-performance supercapacitors. *RSC Advances* 12(20): 12590-12599. <https://doi.org/10.1039/d2ra01658c>

- Luo, J., Meng, X., Crittenden, J., Qu, J., Hu, C., Liu, H. & Peng, P. 2018. Arsenic adsorption on A-MnO₂ nanofibers and the significance of (1 0 0) facet as compared with (1 1 0). *Chemical Engineering Journal* 331: 492-500. <https://doi.org/10.1016/j.cej.2017.08.123>
- Luo, X. & Deng, F. 2019. *Nanomaterials for the Removal of Pollutants and Resource Reutilization*. Elsevier.
- Manuel Stephan, A. & Nahm, K.S. 2006. Review on composite polymer electrolytes for lithium batteries. *Polymer* 47(16): 5952-5964. <https://doi.org/10.1016/j.polymer.2006.05.069>
- Mao, Y., Liu, K., Zhan, C., Geng, L., Chu, B. & Hsiao, B.S. 2017. Characterization of nanocellulose using small-angle neutron, X-ray, and dynamic light scattering techniques. *Journal of Physical Chemistry B* 121(6): 1340-1351. <https://doi.org/10.1021/acs.jpcc.6b11425>
- Meena, M., Sonigra, P. & Yadav, G. 2021. Biological-based methods for the removal of volatile organic compounds (VOCs) and heavy metals. *Environmental Science and Pollution Research* 28(3): 2485-2508. <https://doi.org/10.1007/s11356-020-11112-4>
- Mohammadian, S., Krok, B., Fritzsche, A., Bianco, C., Tosco, T., Cagigal, E., Mata, B., Gonzalez, V., Diez-Ortiz, M., Ramos, V., Montalvo, D., Smolders, E., Sethi, R. & Meckenstock, R.U. 2021. Field-scale demonstration of *in situ* immobilization of heavy metals by injecting iron oxide nanoparticle adsorption barriers in groundwater. *Journal of Contaminant Hydrology* 237: 103741. <https://doi.org/10.1016/j.jconhyd.2020.103741>
- Nandiyanto, Asep Bayu Dani, Risti Ragadhita & Jumril Yunas. 2020. Adsorption isotherm of densed monoclinic tungsten trioxide nanoparticles. *Sains Malaysiana* 49(12): 2881-2890. <https://doi.org/10.17576/jsm-2020-4912-01>
- Ng, J. (Jack), A. Gomez-Camirero, Inter-Organization Programme for the Sound Management of Chemicals, and International Program on Chemical Safety. 2001. *Arsenic and Arsenic Compounds*. World Health Organization.
- Noor Halini Baharim, Fridelina Sjahrir, Rahmad Mohd Taib, Norazlina Idris & Tuan Azmar Tuan Daud. 2023. Methylene blue adsorption by acid post-treated low temperature biochar derived from banana (*Musa acuminata*) pseudo stem. *Sains Malaysiana* 52(2): 547-561. <https://doi.org/10.17576/jsm-2023-5202-17>
- Peydayesh, M., Suta, T., Usuelli, M., Handschin, S., Canelli, G., Bagnani, M. & Mezzenga, R. 2021. Sustainable removal of microplastics and natural organic matter from water by coagulation-flocculation with protein amyloid fibrils. *Environmental Science and Technology* 55(13): 8848-8858. <https://doi.org/10.1021/acs.est.1c01918>
- Pi, H., Wang, R., Ren, B., Zhang, X. & Wu, J. 2018. Facile fabrication of multi-structured SiO₂@PVDF-HFP nanofibrous membranes for enhanced copper ions adsorption. *Polymers* 10(12): 1385. <https://doi.org/10.3390/polym10121385>
- Pramanik, S., Sahu, S.K., Meshram, P. & Pandey, B.D. 2014. Arsenic removal from spent liquor generated during processing of vanadium sludge. *Advanced Materials Research* 828: 55-63. <https://doi.org/10.4028/www.scientific.net/AMR.828.55>
- Puguan, J.M.C., Chung, W.J. & Kim, H. 2016. Synthesis and characterization of electrospun PVdF-HFP/Silane-functionalized ZrO₂ hybrid nanofiber electrolyte with enhanced optical and electrochemical properties. *Solid State Sciences* 62: 34-42. <https://doi.org/10.1016/j.solidstatedsciences.2016.10.010>
- Rahman, H.L., Erdem, H., Sahin, M. & Erdem, M. 2020. Iron-incorporated activated carbon synthesis from biomass mixture for enhanced arsenic adsorption. *Water, Air, and Soil Pollution* 231: 6. <https://doi.org/10.1007/s11270-019-4378-4>
- Ramlah Abd Rashid, Ali H. Jawad, Mohd Azlan Bin Mohd Ishak & Nur Nasulhah Kasim. 2018. FeCl₃-activated carbon developed from coconut leaves: Characterization and application for methylene blue removal. *Sains Malaysiana* 47(3): 603-610. <https://doi.org/10.17576/jsm-2018-4703-22>
- Saif, S., Tahir, A., Asim, T., Chen, Y. & Adil, S.F. 2019. Polymeric nanocomposites of iron-oxide nanoparticles (IONPs) synthesized using *Terminalia chebula* leaf extract for enhanced adsorption of arsenic(v) from water. *Colloids and Interfaces* 3(1): 17. <https://doi.org/10.3390/colloids3010017>
- Saod, W.M., Oliver, I.W., Thompson, D.F., Holborn, S., Contini, A. & Zholobenko, V. 2023. Magnesium oxide loaded mesoporous silica: Synthesis, characterisation and use in removing lead and cadmium from water supplies. *Environmental Nanotechnology, Monitoring and Management* 20: 100817. <https://doi.org/10.1016/j.enmm.2023.100817>
- Schroeder, A.B., Dobson, E.T.A., Rueden, C.T., Tomancak, P., Jug, F. & Eliceiri, K.W. 2021. The ImageJ ecosystem: Open-source software for image visualization, processing, and analysis. *Protein Science* 30(1): 234-249. <https://doi.org/10.1002/pro.3993>
- Shafiq, M., Alazba, A.A. & Amin, M.T. 2018. Removal of heavy metals from wastewater using date palm as a biosorbent: A comparative review. *Sains Malaysiana* 47(1): 35-49. <https://doi.org/10.17576/jsm-2018-4701-05>
- Shi, H., Chen, F., Fu, L., Zhao, S., Zhang, W., Chen, F. & Shi, Q. 2021. Preparation of nano-iron loaded cassava fibre composite material for hexavalent chromium removal. *Sains Malaysiana* 50(11): 3373-3382. <https://doi.org/10.17576/jsm-2021-5011-21>
- Singh, K.P., Gupta, S., Singh, A.K. & Sinha, S. 2011. Optimizing adsorption of crystal violet dye from water by magnetic nanocomposite using response surface modeling approach. *Journal of Hazardous Materials* 186(2-3): 1462-1473. <https://doi.org/10.1016/j.jhazmat.2010.12.032>

- Sinha Ray, S., Lee, H.K., Huyen, D.T.T., Park, Y.I., Park, H., Nam, S.E., Kim, I.C. & Kwon, Y.N. 2021. Fluorine-free anti-droplet surface modification by hexadecyltrimethoxysilane-modified silica nanoparticles-coated carbon nanofibers for self-cleaning applications. *Progress in Organic Coatings* 153: 106165. <https://doi.org/10.1016/j.porgcoat.2021.106165>
- Siti Zu Nurain Ahmad, Wan Norharyati Wan Salleh, Norhaniza Yusof, Mohd Zamri Mohd Yusop, Rafidah Hamdan, Nor Asikin Awang, Nor Hafiza Ismail, Norafiqah Rosman, Norazlianie Sazali & Ahmad Fauzi Ismail. 2021. Pb(II) removal and its adsorption from aqueous solution using zinc oxide/graphene oxide composite. *Chemical Engineering Communications* 208(5): 646-660. <https://doi.org/10.1080/00986445.2020.1715957>
- Su, Y., Burger, C., Hsiao, B.S. & Chu, B. 2014. Characterization of TEMPO-Oxidized cellulose nanofibers in aqueous suspension by small-angle x-ray scattering. *Journal of Applied Crystallography* 47(2): 788-798. <https://doi.org/10.1107/S1600576714005020>
- Tibolla, H., Pelissari, F.M. & Menegalli, F.C. 2014. Cellulose nanofibers produced from banana peel by chemical and enzymatic treatment. *LWT* 59(2P2): 1311-1318. <https://doi.org/10.1016/j.lwt.2014.04.011>
- Torasso, N., Vergara-Rubio, A., Rivas-Rojas, P., Huck-Iriart, C., Larrañaga, A., Fernández-Cirelli, A., Cerveny, S. & Goyanes, S. 2021. Enhancing arsenic adsorption via excellent dispersion of iron oxide nanoparticles inside poly(vinyl alcohol) nanofibers. *Journal of Environmental Chemical Engineering* 9(1): 104664. <https://doi.org/10.1016/j.jece.2020.104664>
- Tripathy, M. & Hota, G. 2020. Maghemite and graphene oxide embedded polyacrylonitrile electrospun nanofiber matrix for remediation of arsenate ions. *ACS Applied Polymer Materials* 2(2): 604-617. <https://doi.org/10.1021/acscpm.9b00982>
- Unuabonah, E.I., Omorogie, M.O. & Oladoja, N.A. 2018. Modeling in adsorption: Fundamentals and applications. In *Composite Nanoadsorbents*, edited by Kyzas, G.Z. & Mitropoulos, A.C. Elsevier. pp. 85-118. <https://doi.org/10.1016/B978-0-12-814132-8.00005-8>
- Veerabhadraiah, A., Ramakrishna, S., Angadi, G., Venkatram, M., Ananthapadmanabha, V.K., NarayanaRao, N.M.H. & Munishamaiah, K. 2017. Development of polyvinyl acetate thin films by electrospinning for sensor applications. *Applied Nanoscience (Switzerland)* 7(7): 355-363. <https://doi.org/10.1007/s13204-017-0576-9>
- Vo, D.T., Do, H.N., Nguyen, T.T., Nguyen, T.T.H., Tran, V.M., Okada, S. & Le, M.L.P. 2019. Sodium ion conducting gel polymer electrolyte using poly(vinylidene fluoride hexafluoropropylene). *Materials Science and Engineering B: Solid-State Materials for Advanced Technology* 241: 27-35. <https://doi.org/10.1016/j.mseb.2019.02.007>
- Wang, Z., Sun, B., Lu, X., Wang, C. & Su, Z. 2019. Molecular orientation in individual electrospun nanofibers studied by polarized AFM-IR. *Macromolecules* 52(24): 9639-9645. <https://doi.org/10.1021/acs.macromol.9b01778>
- Xie, X., Lu, C., Xu, R., Yang, X., Yan, L. & Su, C. 2022. Arsenic removal by manganese-doped mesoporous iron oxides from groundwater: Performance and mechanism. *Science of the Total Environment* 806(Part 2): 150615. <https://doi.org/10.1016/j.scitotenv.2021.150615>
- Xiong, C., Wang, W., Tan, F., Luo, F., Chen, J. & Qiao, X. 2015. Investigation on the efficiency and mechanism of Cd(II) and Pb(II) removal from aqueous solutions using MgO nanoparticles. *Journal of Hazardous Materials* 299: 664-674. <https://doi.org/10.1016/j.jhazmat.2015.08.008>
- Yalcinkaya, F., Yalcinkaya, B. & Jirsak, O. 2015. Dependent and independent parameters of needleless electrospinning. In *Vlakna a Textil*. Slovak University of Technology in Bratislava. pp. 75-79. <https://doi.org/10.5772/65838>
- Yavari, M., Ebadi, F., Meloni, S., Wang, Z.S., Yang, T.C.J., Sun, S., Schwartz, H., Wang, Z., Niesen, B., Durantini, J., Rieder, P., Tvingstedt, K., Buonassisi, T., Choy, W.C.H., Filippetti, A., Dittrich, T., Olthof, S., Correa-Baena, J-P. & Tress, W. 2019. How far does the defect tolerance of lead-halide perovskites range? The example of Bi impurities introducing efficient recombination centers. *Journal of Materials Chemistry A* 7(41): 23838-23853. <https://doi.org/10.1039/c9ta01744e>
- Zhang, C.L. & Yu, S.H. 2014. Nanoparticles meet electrospinning: Recent advances and future prospects. *Chemical Society Reviews* 43(13): 4423-4448. <https://doi.org/10.1039/c3cs60426h>
- Zhang, C., Uchikoshi, T., Ichinose, I. & Liu, L. 2019. Surface modification on cellulose nanofibers by TiO₂ coating for achieving high capture efficiency of nanoparticles. *Coatings* 9(2): 139. <https://doi.org/10.3390/COATINGS9020139>
- Zhang, H., Hu, J., Xie, J., Wang, S. & Cao, Y. 2019. A solid-state chemical method for synthesizing MgO nanoparticles with superior adsorption properties. *RSC Advances* 9(4): 2011-2017. <https://doi.org/10.1039/C8RA09199D>
- Zhao, Y., Yuan, X., Li, X., Jiang, L. & Wang, H. 2021. Burgeoning prospects of biochar and its composite in persulfate-advanced oxidation process. *Journal of Hazardous Materials* 409: 124893. <https://doi.org/10.1016/j.jhazmat.2020.124893>
- Zhu, Y., Zheng, L., Liu, W., Qin, L. & Ngai, T. 2020. Poly(l-Lactic Acid) (PLLA)/MgSO₄·7H₂O composite coating on magnesium substrates for corrosion protection and cytocompatibility promotion. *ACS Applied Bio Materials* 3(3): 1364-1373. <https://doi.org/10.1021/acscbm.9b00983>

*Corresponding author; email: asna002@brin.go.id

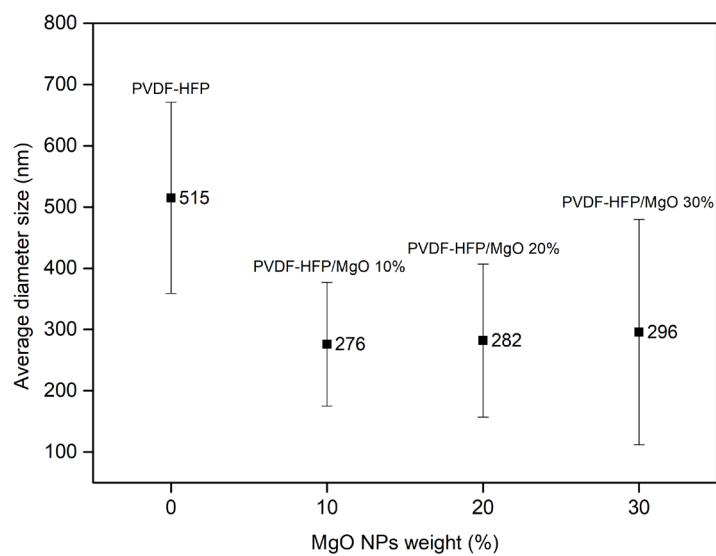


FIGURE S1. Graph of the relationship between the percentage of MgO nanoparticles in nanofiber and the average diameter of the nanofiber

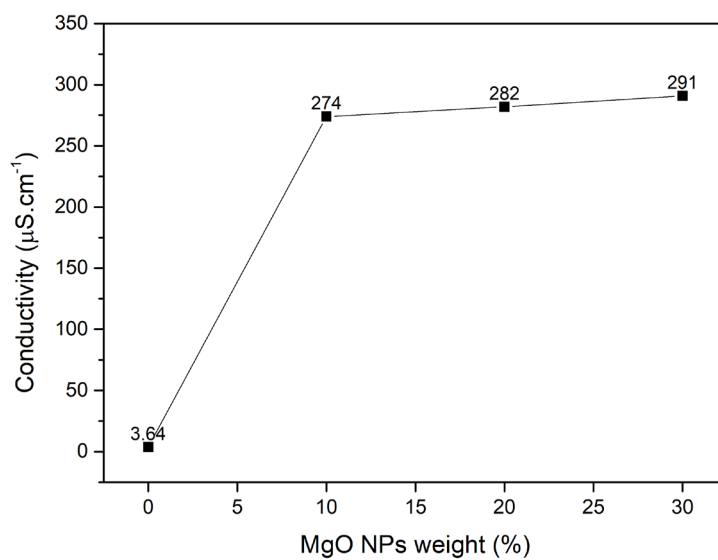


FIGURE S2. Relationship between the weight percentage of MgO nanoparticles and the conductivity of the resulting solution

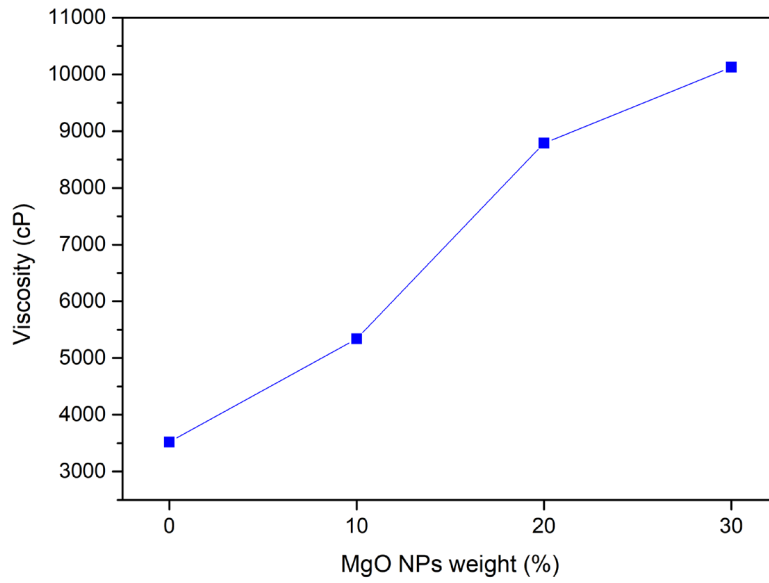


FIGURE S3. Relationship between the weight percentage of MgO nanoparticles and the viscosity of the resulting solution

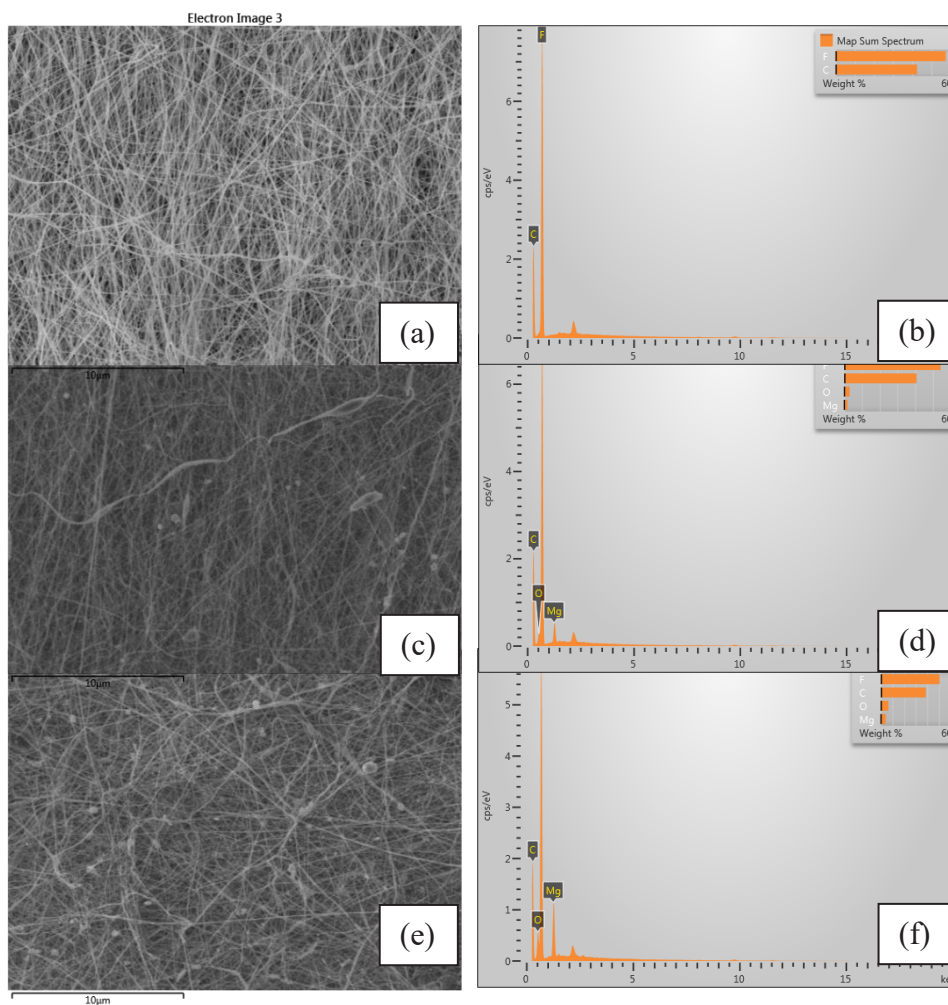


FIGURE S4. Scanned sample areas and EDS spectra for (a) and (b) pure PVDF-HFP nanofibers, (c) and (d) 10% (w/w) PVDF-HFP/MgO nanofiber composites, (e) and (f) 30% (w/w) PVDF-HFP/MgO nanofiber composites

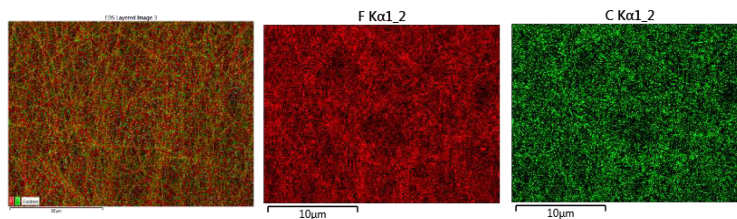


FIGURE S5. EDS mapping of pure PVDF-HFP nanofiber

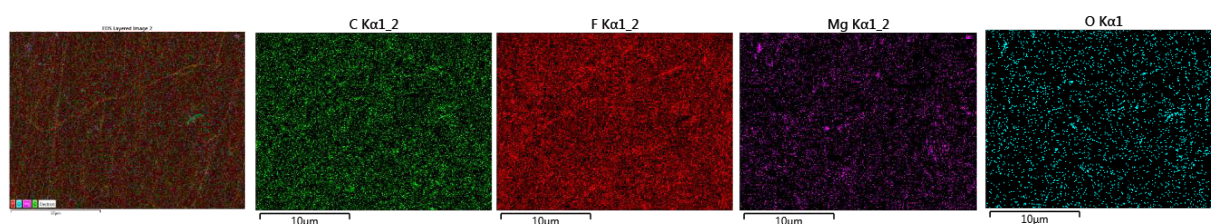


FIGURE S6. EDS Mapping of PVDF-HFP/MgO 10% (w/w) nanofiber composites

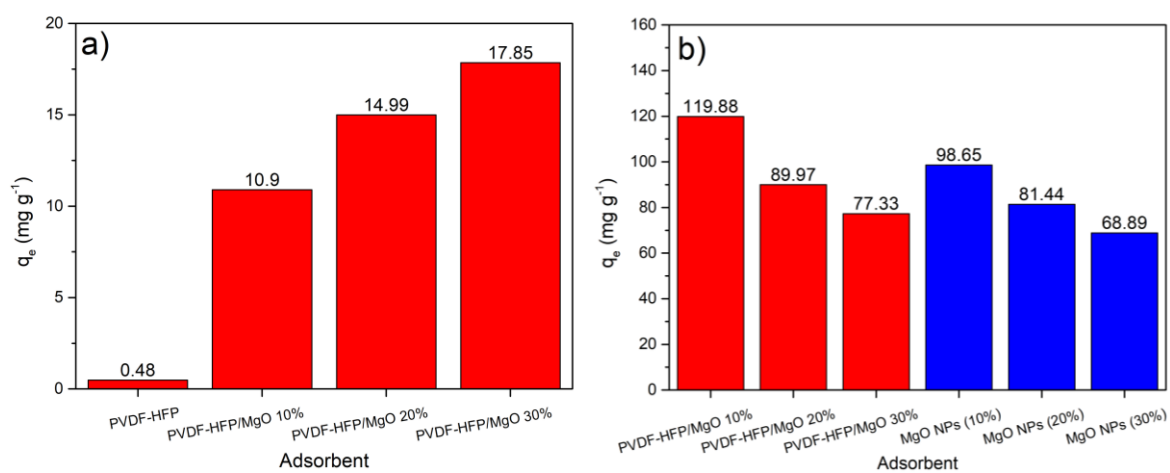


FIGURE S7. Preliminary study of the adsorption ability of MgO nanoparticles, pure PVDF-HFP nanofiber, and PVDF-HFP/MgO nanofiber composites with (a) the value of the q_e based on the total weight of the adsorbent and (b) the value of the q_e based on the weight of the MgO NPs

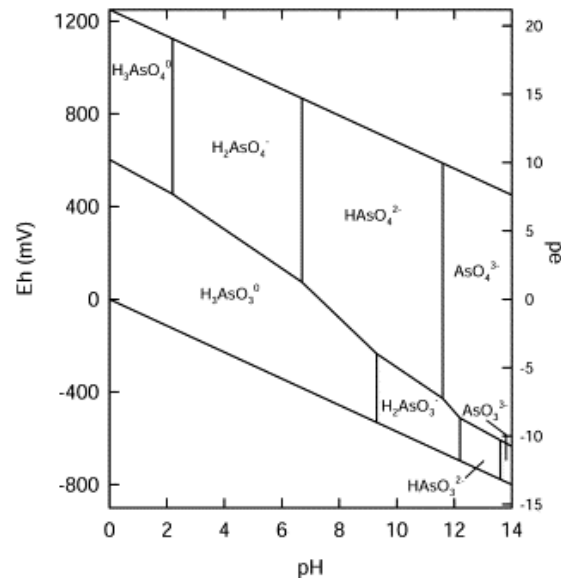


FIGURE S8. Eh-pH diagram of arsenic species (Pramanik et al. 2014)

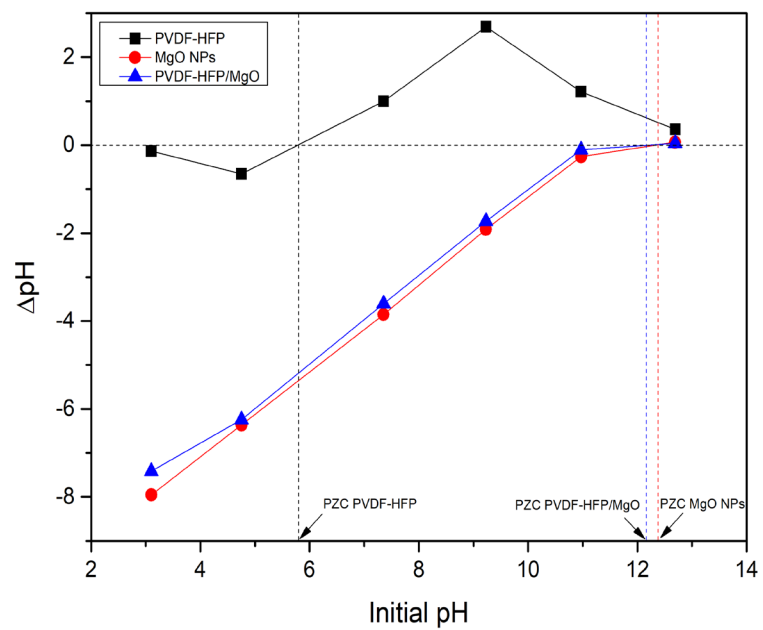


FIGURE S9. Graph of determining the point zero charge (PZC) value of pure PVDF-HFP nanofiber, MgO nanoparticles, and PVDF-HFP/MgO nanofiber composites

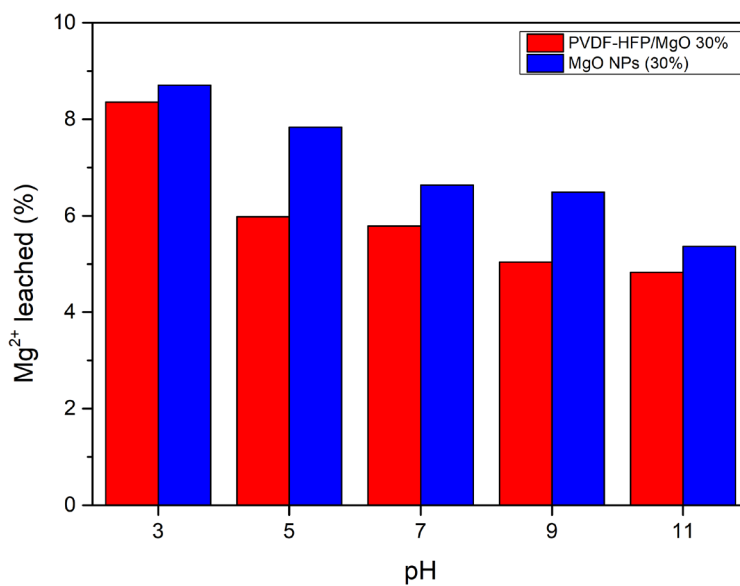


FIGURE S10. Graph of the effect of pH on the amount of Mg^{2+} leached on PVDF-HFP/MgO nanofiber composites and MgO nanoparticles

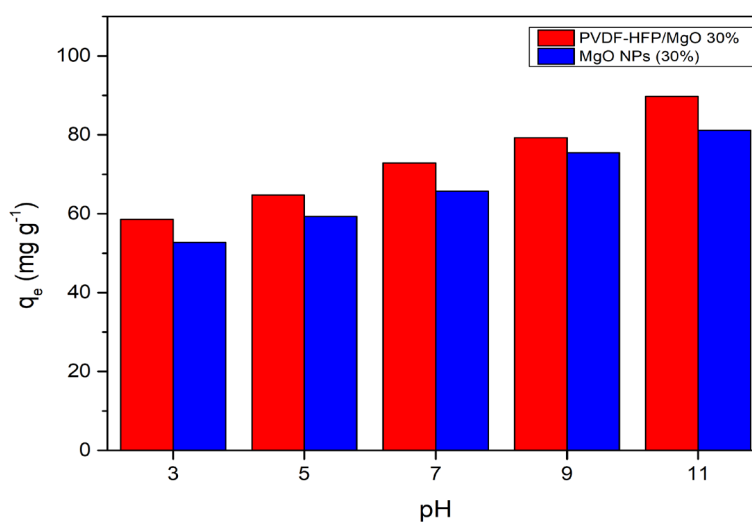


FIGURE S11. Effect of adsorbate pH on the adsorption capacity of PVDF-HFP/MgO nanofiber composites and bare MgO nanoparticles with the value of the q_e based on the weight of the MgO NPs

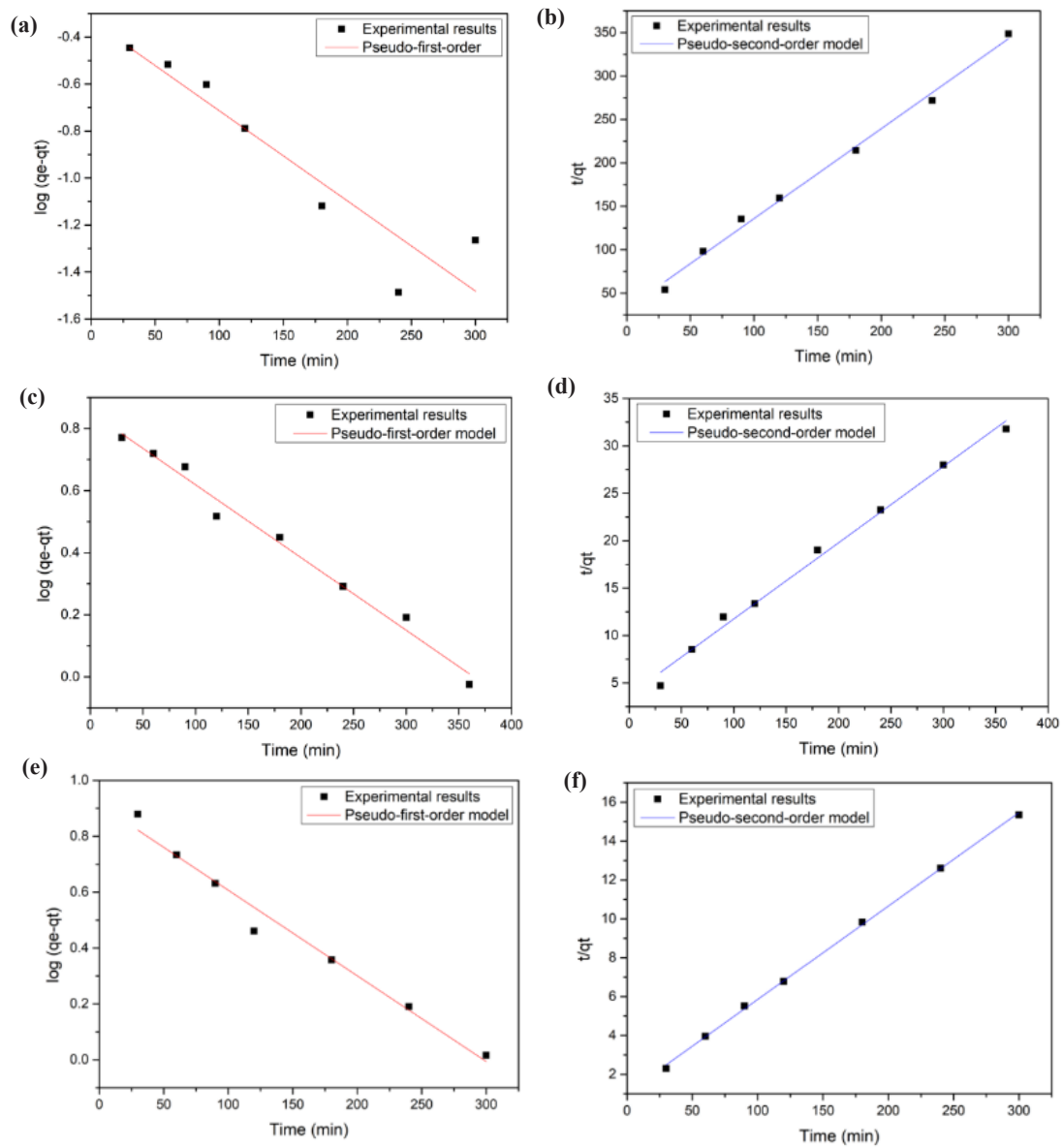


FIGURE S12. Adsorption kinetics model of pseudo-first-order and pseudo-second-order (a-b) pure PVDF-HFP nanofibers, (c-d) PVDF-HFP/MgO 10% composite nanofiber, and (e-f) PVDF-HFP/MgO 30% composite nanofiber to As(V)

TABLE S1. Adsorption kinetic parameters of As(V)

Adsorbent	$q_e \text{ exp (mg g}^{-1}\text{)}$	Pseudo First Order		Pseudo Second Order			
		k_1 (min^{-1})	R^2	q_e (mg g^{-1})	k_2 (g mg^{-1} min^{-1})	R^2	q_e (mg g^{-1})
PVDF-HFP	0.92	0.00884	0.878	0.47	0.03333	0.995	0.97
PVDF-HFP/MgO 10%	12.27	0.00540	0.986	7.13	0.00174	0.993	12.49
PVDF-HFP/MgO 30%	20.59	0.00706	0.980	8.20	0.00221	0.999	20.81

TABLE S2. Parameters of Langmuir and Freundlich adsorption isotherms of pure PVDF-HFP nanofiber, PVDF-HFP/MgO 10% composite nanofiber, and PVDF-HFP/MgO 30% composite nanofiber

Adsorbent sample	Langmuir			Freundlich		
	q_{\max} (mg g ⁻¹)	K_L (L mg ⁻¹)	R^2	1/n	K_F (mg g ⁻¹)(L mg ⁻¹) ^{1/n}	R^2
PVDF-HFP	1.62	0.0152	0.993	0.536	0.081	0.976
PVDF-HFP/MgO 10%	18.69	0.0425	0.990	0.379	2.665	0.880
PVDF-HFP/MgO 30%	41.47	3.1765	0.984	0.067	31.123	0.929

TABLE S3. Comparison of As(V) adsorption capacity of various adsorbents

Adsorbent(s)	q_{\max} (mg g ⁻¹)	References
PVDF-HFP/MgO nanofiber	41.47	This study
α -MnO ₂ nanofiber	60.9	Luo et al. (2018)
PVA-iron oxide nanofiber	52	Torasso et al. (2021)
PAN/GO/ γ -Fe ₂ O ₃ nanofiber	36.1	Tripathy & Hota (2020)
MOF hybrid nanofiber	42.17	Guo et al. (2021)
Nanochitosan	13	Kwok et al. (2018)
Iron-incorporated activated carbon	42.92	Rahman et al. (2020)
HA/Fe-Mn oxides-loaded biochar	35.59	Guo et al. (2019)
Fe/Cu nanoparticles	21.32	Babaei et al. (2018)
ZnO-impregnated corncob biochar	25.9	Cruz et al. (2020)
PVA-alginate-supported IONPs	40.3	Saif et al. (2019)
Fe-Mn bimetallic oxides	38.09	Xie et al. (2022)